Some Expectations for Submesoscale Sea Surface Height Variance Spectra

JÖRN CALLIES

California Institute of Technology, Pasadena, California

WEIGUANG WU

University of California San Diego, La Jolla, California

ABSTRACT

In anticipation of the Surface Water and Ocean Topography (SWOT) wide-swath altimetry mission, this study reviews expectations for sea surface height (SSH) variance spectra at wavelengths of 10–100 km. Kinetic energy spectra from in situ observations and numerical simulations indicate that SSH variance spectra associated with balanced flow drop off steeply with wavenumber, with at least the negative fourth power of the wavenumber. Such a steep drop-off implies that even drastic reductions in altimetry noise yield only a modest improvement in the resolution of balanced flow. This general expectation is made concrete by extrapolating SSH variance spectra from existing altimetry to submesoscales, the results of which suggest that in the extratropics (poleward of 20° latitude) SWOT will improve the resolution from currently about 100 km to a median of 51 or 74 km, depending on whether or not submesoscale balanced flows are energetic. Internal waves, in contrast to balanced flow, give rise to SSH variance spectra that drop off relatively gently with wavenumber, so SSH variance should become strongly dominated by internal waves in the submesoscale range. In situ observations of the internal-wave field suggest that the internal-wave signal accessible by SWOT will be largely dominated by internal tides. The internal-wave continuum is estimated to have a spectral level close to but somewhat lower than SWOT's expected noise level.

1. Introduction

Since the breakthrough TOPEX/Poseidon mission launched in 1992, satellite altimetry has been used with great success to characterize the ocean circulation. Mesoscale geostrophic eddies, by far the most energetic features of the ocean circulation, are now routinely mapped with near-global coverage (e.g., Wunsch and Stammer 1998; Stammer and Cazenave 2017). Altimetry has given insight into the energy, scale, and propagation of eddies (e.g., Chelton et al. 2011; Tulloch et al. 2011) and into the tracer transport effected by eddy stirring (e.g., Stammer 1998; Marshall et al. 2006; Abernathey and Marshall 2013). Altimetry has also been instrumental in obtaining accurate global maps of the external tide (e.g., Egbert et al. 1994; Stammer et al. 2014) and in constraining the energy losses of the external tide to internal tides and dissipation (Egbert and Ray 2000).

The spatial resolution of the presently used nadir altimetry is generally limited to about 100 km (all scales are given as wavelengths; cf. Fig. 5), a consequence of the spectral level of the white-noise floor on the order of $100 \, \text{cm}^2 \, \text{cpkm}^{-1}$ (where cpkm is cycles per kilometer). The Surface Water and Ocean Topography (SWOT) mission, scheduled for launch in 2021, is expected to lower the noise floor by a factor of 50 to about $2 \, \text{cm}^2 \, \text{cpkm}^{-1}$ (Desai et al. 2018). This substantial reduction in noise will allow SWOT to resolve smaller-scale features in the sea surface height (SSH) field, opening up the prospect of observing submesoscale fronts and filaments globally (e.g., Fu and Ferrari 2008). By how much SWOT's resolution will improve compared to nadir altimetry, however, depends critically on how strong the signal is at submesoscales. (We here use the term "submesoscale" to designate the range of scales smaller than the energy-dominating mesoscale eddies, with no implication of high-Rossby-number dynamics.)

In the past few years, quite a bit has been learned about the dynamics at 10–100 km, the part of the submesoscale range potentially accessible by SWOT. Modeling, in situ observations, and theory have revealed that balanced submesoscale flow is energized primarily

Corresponding author: Jörn Callies, jcallies@caltech.edu

by baroclinic instabilities in deep winter mixed layers (e.g., Boccaletti et al. 2007; Mensa et al. 2013; Sasaki et al. 2014; Callies et al. 2015, 2016), and that internal waves can make important contributions to the submesoscale energy (e.g., Chavanne and Klein 2010; Ray and Zaron 2011; Richman et al. 2012; Callies and Ferrari 2013; Bühler et al. 2014; Rocha et al. 2016a; Savage et al. 2017b; Qiu et al. 2017). Building on these advances, we here extrapolate the existing nadir altimetry observations of balanced flow to submesoscales, and we present a prediction of the SSH signal due to the internal-wave continuum. Our analysis provides predictions for the spatial scales accessible by SWOT and for what types of motion might dominate the SWOT signal.

2. General expectations

Motion at spatial scales of 10–100 km can have important contributions from both balanced flow and internal waves.[1] The internal-wave field in turn consists of three distinct components: near-inertial waves, internal tides, and the internal-wave continuum. Near-inertial waves are expected to have only a small signature in SSH (e.g., Munk and Phillips 1968; Fu 1981), so they will unlikely be part of the signal obtained by SWOT; we will not discuss them any further. Internal tides and the internal-wave continuum, on the other hand, do have leading-order SSH signatures for frequencies away from the local inertial frequency. In the following, we therefore discuss general expectations for submesoscale SSH variance spectra from balanced flow, internal tides, and the internal-wave continuum.

It is crucial to distinguish between SSH signals due to these different types of motion. Directly inferring surface velocities from SSH snapshots—without assuming anything about the flow's vertical structure—is possible only for geostrophically balanced flow. The different types of motion also have drastically different impacts on the transport of tracers and momentum: balanced flow tends to be strongly nonlinear at mesoscales and submesoscales and thus lead to vigorous stirring and turbulent transport, whereas internal waves are typically linear to leading order and cause irreversible mixing only when they overturn and induce small-scale turbulence.

a. Balanced flow

Submesoscale balanced flows have received increased attention over the past decade (e.g., Capet et al. 2008;

Thomas et al. 2008; McWilliams 2016). Their importance is thought to lie primarily in their ability to restratify the upper ocean (e.g., Lapeyre and Klein 2006; Fox-Kemper et al. 2011) and to exchange water between the surface and interior ocean (e.g., Klein and Lapeyre 2009; Ferrari 2011). These processes are thought to affect the ocean's uptake and transport of heat, carbon, and other tracers (e.g., Lévy et al. 2012; Mahadevan 2014), they possibly feed back on the stratification and circulation of the large-scale ocean (Lévy et al. 2010), and they may play a central role in structuring the ecosystems of the upper ocean (Lévy et al. 2018).

Both in situ observations and numerical models show that submesoscale balanced flows are most energetic in deep winter mixed layers, while they are much less vigorous in the seasonal thermocline in summer and in the permanent thermocline year-round (Mensa et al. 2013; Sasaki et al. 2014; Callies et al. 2015; Thompson et al. 2016; Su et al. 2018). This enhancement in deep winter mixed layers suggests that the submesoscales are energized primarily by baroclinic mixed layer instabilities (Boccaletti et al. 2007; Fox-Kemper and Ferrari 2008; Callies et al. 2016). These instabilities laterally slide light over dense water, generating submesoscale kinetic energy by tapping into available potential energy provided by steeply sloping isopycnals in the mixed layer. This potential energy is set up by a combination of the lateral buoyancy gradients of baroclinic mesoscale eddies and the vertical mixing achieved by atmospherically forced mixed layer turbulence. The amount of potential energy available for release is much larger in winter, when atmospherically forced turbulence is strong and mixed layers are deep. The seasonal cycle of the mixed layer therefore entails a seasonal cycle in baroclinic mixed layer instabilities and thus in submesoscale energy levels.

The conversion from potential to kinetic energy occurs at submesoscale instability scales of order 1–10 km (Boccaletti et al. 2007). Subsequently, turbulent scale interactions preferentially transfer the energy back to larger scales and energize the entire submesoscale range (Sasaki et al. 2014; Callies et al. 2016). The result of this wintertime energization is a kinetic energy spectrum that tends to fall off like k^{-2} over the 10–100-km range (Shcherbina et al. 2013; Callies et al. 2015), where k is the wavenumber along a one-dimensional track. In summer, on the other hand, when the submesoscale energization is absent, the near-surface kinetic energy spectrum of balanced flow tends to be significantly steeper, falling off like k^{-3} (Wang et al. 2010; Callies and Ferrari 2013; Callies et al. 2015; Rocha et al. 2016a).

The k^{-3} kinetic energy spectrum of the "weak submesoscales" regime is typically attributed to interior

---

[1] Unbalanced turbulence has scales of order 1 km and smaller (e.g., Klymak and Moum 2007), so it is not expected to contribute appreciably to the signal in the scale range of interest here.
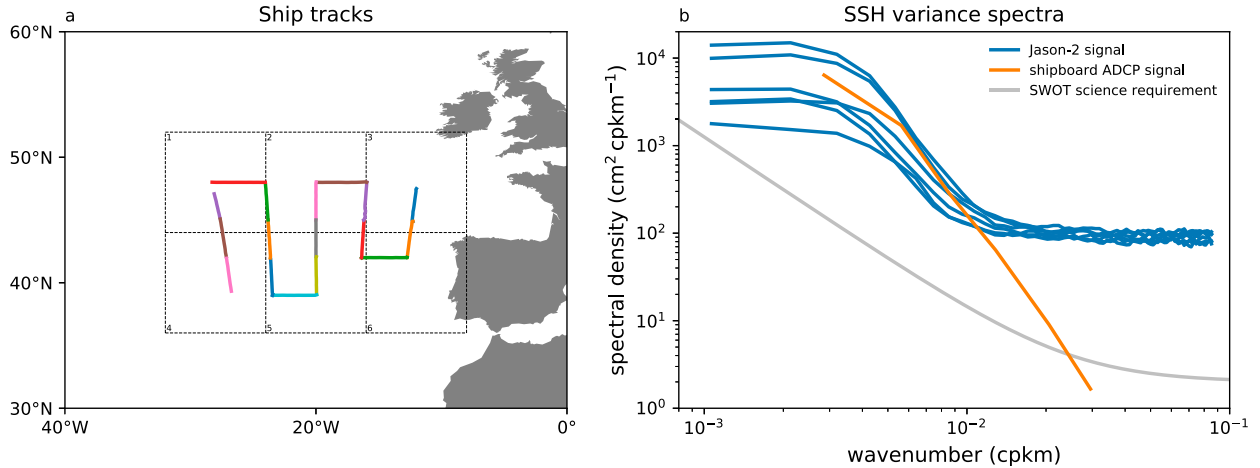
FIG. 1. Example of the rapid drop-off of SSH variance spectra due to balanced submesoscale flows. (a) The locations of ship tracks (colored lines) and the $8° \times 8°$ regions from which *Jason-2* wavenumber spectra are computed. (b) The wavenumber SSH variance spectrum converted from shipboard ADCP data assuming geostrophic balance (orange line) and the *Jason-2* spectra from the six $8° \times 8°$ regions (blue lines). The gray line is SWOT's expected error spectrum.

geostrophic turbulence, which produces this power law in an inertial range in which potential enstrophy cascades to small scales (Charney 1971). The k^{-2} spectrum of the ''strong submesoscales'' regime signifies more energy at submesoscales, but the origin of the power law is less clear. Energy injection by baroclinic mixed layer instabilities and turbulent transfer to larger scales clearly play a role (Sasaki et al. 2014; Callies et al. 2016), but it is unlikely that classic turbulence theory is applicable (see further discussion in Callies and Ferrari 2018). Irrespective of the reason, however, the available evidence from models and in situ data suggests that the k^{-2} spectrum in this regime is fairly universal (e.g., Capet et al. 2008; Sasaki and Klein 2012; Callies et al. 2015). Kinetic energy spectra falling off much more gently than k^{-2} in the submesoscale range have been found in neither observations nor models.

At scales of 10–100 km, the submesoscale flows generated by baroclinic mixed layer instabilities are to leading order in geostrophic balance (e.g., Callies et al. 2015). As geostrophic balance relates the horizontal surface velocity to SSH gradients, SSH variance spectra are proportional to k^{-2} times the corresponding kinetic energy spectra. The strong submesoscales regime with a k^{-2} kinetic energy spectrum thus has a k^{-4} SSH variance spectrum; the weak submesoscales regime with a k^{-3} kinetic energy spectrum has a k^{-5} SSH variance spectrum.

In situ velocity observations from the eastern North Atlantic illustrate this steep drop-off (Fig. 1). Shipboard ADCP data yield a near-surface kinetic energy spectrum that falls off roughly like k^{-2} at scales smaller than 200 km (see appendix A for details). A Helmholtz

decomposition (Bühler et al. 2014) indicates that the flow is predominantly rotational and thus likely geostrophic (not shown). The observed flow appears to be in the strong submesoscales regime. Geostrophic balance allows us to convert the cross-track component of the observed kinetic energy spectrum to an estimate of the along-track SSH variance spectrum:

$$|\hat{h}|^2 = \frac{f^2}{g^2 k^2} |\hat{v}|^2. \tag{1}$$

At scales larger than 100 km, the spectrum inferred from the ADCP data is broadly consistent with SSH variance spectra obtained from *Jason-2* along-track data from the same region (Fig. 1). At smaller scales, the *Jason-2* data are compromised by the measurement noise; the spectra flatten out and become white. The ADCP data instead resolve these submesoscales and suggest that the true SSH variance spectrum of the balanced flow drops off steeply, roughly like k^{-4}.

These steep SSH variance spectra and the correspondingly smooth SSH fields make the task of resolving submesoscale balanced flow rather challenging, even in the strong submesoscales regime. If we define the resolution as the wavelength at which the wavenumber spectrum of the signal intersects the wavenumber spectrum of the measurement error, we find that improving the resolution by an order of magnitude requires lowering the noise level by four orders of magnitude. Given the expected 50-fold decrease in the noise level in going from nadir altimetry to SWOT, we should expect the resolution to improve by a factor of $50^{1/4} = 2.7$—for example, from 100 to 38 km. In the weak

submesoscales regime, the resolution would improve by a factor of $50^{1/5} = 2.2$—for example, from 100 to 46 km.

These scaling laws based on spectral slopes inferred from observed and simulated kinetic energy spectra give good guidance on the expected resolution increase for the balanced flow. In section 3, we combine these ideas with existing nadir altimetry to obtain a quantitative assessment of the expected SWOT resolution scale for balanced flow across the global ocean. This assessment takes into account the geographically variable energy levels and the shape of SWOT's expected noise spectrum, which is not entirely white.

b. Internal tides

Internal tides are internal waves that are generated when tidal currents pass over an uneven seafloor in a stratified ocean (e.g., Garrett and Kunze 2007). These waves have frequencies set by the tidal forcing, predominantly semidiurnal and diurnal. The global energy conversion rate from external to internal tides amounts to about 1 TW (Egbert and Ray 2003), a substantial fraction of which is thought to be dissipated by small-scale mixing in the deep ocean—and thus to contribute to water mass transformation that is crucial for the large-scale overturning circulation (e.g., Munk and Wunsch 1998).

Despite their name, internal tides have a signature in SSH (e.g., Wunsch and Gill 1976; Gill 1982; Wunsch 2013; Kelly 2016). The linear dynamics of internal tides are conveniently described in terms of rigid-lid, flat-bottom vertical modes, which are defined by the Sturm–Liouville problem:

$$\frac{d}{dz}\left(\frac{1}{N^2}\frac{dF}{dz}\right) + \frac{1}{c^2}\,F = 0,$$
$$\frac{dF}{dz} = 0 \quad \text{at} \quad z = 0 \quad \text{and} \quad z = -H, \qquad (2)$$

where N is the buoyancy frequency and H the depth of the ocean. This defines a discrete set of modes F_n with eigenvalues $-1/c_n^2$. The modes F_n describe the vertical structure of the pressure field and of the horizontal velocities. The $n = 0$ mode is barotropic—F_0 is constant and $c_0 = \infty$ because we applied the rigid-lid approximation. The $n \geq 1$ modes are baroclinic and ordered such that the nth mode has n zero crossings. We calculate these modes from the ECCO version 4 interpolated climatology (Forget et al. 2015; see appendix B for details).

In an ocean with a rigid lid, a flat bottom, and a constant inertial frequency f, the linear equations of motion in the hydrostatic limit, applied to a horizontally planar wave and projected onto the nth baroclinic mode, yield the dispersion relation

$$\omega^2 = f^2 + c_n^2\kappa^2, \qquad (3)$$

where $\kappa = (k^2 + l^2)^{1/2}$ is the magnitude of the horizontal wavenumber vector with components k and l. For internal tides, the frequency ω is determined by the astronomical forcing, so the dispersion relation defines a set of discrete wavenumbers $\kappa_n = (\omega^2 - f^2)^{1/2}/c_n$. While in reality the seafloor is not flat—otherwise internal tides would not be generated in the first place—internal tides still have their energy concentrated around this set of discrete wavenumbers (e.g., Ray and Mitchum 1997; Ray and Zaron 2016; Zaron 2017).

Globally, most of the tidal SSH variance is semidiurnal. (For the purpose of this study, we make no distinction between the lunar and solar constituents.) The semidiurnal mode-1 wavenumber κ_1 is on the order of 100 km, with substantial global variation due to changes in depth, stratification, and the inertial frequency (Fig. B1). Where the internal tide is strong compared to both the balanced flow and the measurement noise, peaks around κ_1 (and sometimes κ_2) can be observed in along-track nadir altimetry (e.g., Ray and Mitchum 1997; Ray and Zaron 2016; Fig. 3). These peaks are broadened by variations in stratification and ocean depth along the track and by the fact that tracks may cut through waves at oblique angles. But distinct peaks are observed nevertheless.

Estimates of the SSH signal associated with internal tides have been obtained by harmonic or spectral analysis of the existing (strongly aliased) altimetry record (e.g., Kantha and Tierney 1997; Dushaw et al. 2011; Zhao et al. 2016; Ray and Zaron 2016) and by forcing tides in numerical simulations (e.g., Arbic et al. 2004; Simmons et al. 2004; Richman et al. 2012; Savage et al. 2017a). The geography of internal-tide amplitudes is complex because internal tides depend on the strength of the external tide, the bottom topography, and their (sometimes long-distance) propagation. Aspects of the global pattern of SSH amplitudes (e.g., Savage et al. 2017a), however, can be understood with simple wave dynamics: the amplitude decreases drastically away from the tropics because internal tides have a weaker SSH signature the closer they are to their turning latitude (cf. Dushaw and Worcester 1998; Qiu et al. 2018). The SSH signature for an internal tide with a given kinetic energy also depends on the stratification profile, which may explain some of the zonal asymmetries seen in SSH amplitudes (see appendix C for details).

For the purpose of discriminating between internal tides and balanced flow, internal tides are often separated into a component that is phase-locked with the astronomical forcing and a residual component that is not (often referred to as "stationary" and "non-stationary"; e.g., Ray and Zaron 2011; Ponte et al. 2017; Qiu et al. 2018).

If internal tides existed in an otherwise steady and resting ocean, they would be perfectly in phase with the astronomical forcing. But the seasonal cycle, mesoscale eddies, and other transients introduce time dependence into the medium through which internal tides propagate (e.g., Rainville and Pinkel 2006; Zaron and Egbert 2014; Zhao 2016). This slightly shifts the (Eulerian) frequency away from that of the astronomical forcing and thus broadens the tidal peak in frequency space. The phase-locked component is typically determined by a harmonic fit to the altimetry record. The residual component is much harder to distinguish from nontidal signals. Its contribution to the full tidal signal has been mapped out recently using both models and along-track altimetry data (Savage et al. 2017a; Zaron 2017).

c. Internal-wave continuum

Besides internal tides (and near-inertial waves), the ocean features a broadband wave field at frequencies between f and N (e.g., Garrett and Munk 1979). This internal-wave continuum is energized by high-frequency wind perturbations, by energy transfer through wave–wave interaction, and possibly by spontaneous and stimulated generation by balanced flow (e.g., Garrett 1979; Ferrari and Wunsch 2009). The internal-wave continuum is generally understood as a field of weakly interacting nearly linear waves.

While the internal-wave continuum is not thought to contribute significantly to the SSH signals retrieved by currently available satellite altimeters, we can anticipate high-frequency internal waves to dominate the SSH variance at small scales. As explained below, the SSH signature of internal waves is expected to fall off much more gently with wavenumber than that of balanced flow because high-frequency waves are amplified in SSH compared to balanced flow with the same kinetic energy.

The linear f-plane momentum equations of a horizontal plane wave at the sea surface ($\hat{h} = \hat{p}/\rho_0 g$) are

$$-i\omega\hat{u} - f\hat{v} = -ikg\hat{h}, \quad (4)$$

$$-i\omega\hat{v} + f\hat{u} = -ilg\hat{h}, \quad (5)$$

and combining these two equations allows us to relate the SSH variance and kinetic energy spectra:

$$\frac{g^2}{f^2}\kappa^2|\hat{h}|^2 = \frac{(\omega^2 - f^2)^2}{f^2(\omega^2 + f^2)}(|\hat{u}|^2 + |\hat{v}|^2). \quad (6)$$

In the low-frequency limit ($\omega \ll f$), this reverts to the familiar relation for geostrophic flow. For inertial flow ($\omega = f$), the SSH signature vanishes. In the high-frequency limit ($\omega \gg f$), the SSH signature is amplified

compared to that of geostrophic flow by a factor ω^2/f^2. It is this amplification that suggests the internal-wave continuum dominates SSH spectra at small scales.

Garrett and Munk (1972) found the internal-wave continuum to be remarkably invariant across the ocean if its amplitude is scaled by $N^{-1/2}$, following expectations from WKB theory. Garrett and Munk (1972, 1975) and Munk (1981) set forth an empirical spectrum to describe the energy level and distribution across frequency and wavenumber space. This spectrum captures the observed internal-wave continuum globally to within a factor of 2 or 3. Deviations, though detectable almost everywhere, are relatively minor (e.g., Polzin and Lvov 2011).

The Garrett–Munk (GM) spectrum is based on a WKB scaling, was devised to apply to the ocean interior, and is least constrained for the low vertical modes that dominate the SSH signal. Extracting a prediction for the SSH variance spectrum thus takes the GM spectrum beyond its intended domain of application, and such a prediction should be taken with a good pinch of salt. We still deem such a prediction useful, however, to get an order of magnitude estimate for the SSH variance spectrum and to understand its high-wavenumber behavior. We refine this prediction with an observationally based estimate in section 4.

In the version of Munk (1981), the kinetic energy spectrum is given by

$$\frac{1}{2}(|\hat{u}|^2 + |\hat{v}|^2)(\omega, n) = \frac{1}{2}d^2 N_0 N\frac{\omega^2 + f^2}{\omega^2}E_0 B(\omega)H(n), \quad (7)$$

where

$$B(\omega) = \frac{2}{\pi}\frac{f}{\omega}(\omega^2 - f^2)^{-1/2}, \quad (8)$$

and

$$H(n) = \frac{(n^2 + n_*^2)^{-1}}{\sum_{j=1}^{\infty}(j^2 + n_*^2)^{-1}}. \quad (9)$$

The overall energy level is set by the dimensionless constant $E_0 = 6.5 \times 10^{-5}$. The stratification is assumed to be exponential, $N = N_0 \exp(z/d)$; the surface-extrapolated buoyancy frequency is $N_0 = 5.2 \times 10^{-3}\,\text{s}^{-1}$, and the e-folding scale is $d = 1300\,\text{m}$. The distribution of energy across vertical modes is set by $H(n)$, with $n_* = 3$ controlling the energy content of the lowest modes. The kinetic energy spectrum can be converted to a wavenumber spectrum of SSH variance by using (6), by applying the dispersion relation (3) with the WKB phase speed $c_n = N_0 d/\pi n$ to convert from frequency to wavenumber space, and by summing over all vertical modes. The result is an SSH variance spectrum that falls off like

κ^{-2} in the high-wavenumber limit—or k^{-2} for the one-dimensional along-track spectrum (Fig. 2).

The GM spectrum thus suggests that the SSH variance spectrum of the internal-wave continuum has the same power-law drop-off as the kinetic energy spectrum, which also falls of like k^{-2}. This contrasts with the balanced flow, for which the SSH variance spectrum is much steeper than the kinetic energy spectrum. The more gentle roll-off of the internal-wave signal suggests that it inevitably dominates the SSH variance at sufficiently small scales.

The question then is whether or not this transition to an SSH signal dominated by the internal-wave continuum will be resolved by SWOT. It is a mission requirement that the wavenumber spectrum of SWOT's error variance does not exceed (Desai et al. 2018)

$$R(k) = \mathcal{N}_0 + \mathcal{N}_1 k^{-2}, \quad \text{where}$$
$$\mathcal{N}_0 = 2\,\text{cm}^2\,\text{cpkm}^{-1} \quad \text{and}$$
$$\mathcal{N}_1 = 1.25 \times 10^{-3}\,\text{cm}^2\,\text{cpkm}. \tag{10}$$

This error spectrum consists of an uncorrelated part that is white in wavenumber space, and a part that exhibits along-track correlation and thus appears red in wavenumber space. In the following, we will take this science requirement as an estimate for SWOT's actual noise level (cf. Esteban Fernandez et al. 2017).

The GM prediction suggests that the internal-wave continuum will not be resolved by SWOT, at least not in the typical case represented by standard parameters (Fig. 2). The SSH variance level predicted by the GM spectrum with $N = N_0$ falls below SWOT's expected error spectrum, with little latitudinal variation, suggesting the internal-wave continuum will make a subdominant contribution to the signal expected for SWOT. It should be noted, however, that the GM prediction depends linearly on the surface stratification, such that it is not inconceivable that the internal-wave continuum will make a significant contribution to the SWOT signal in locations and times of strong surface stratification (cf. Rocha et al. 2016b).

Motivated by the significant uncertainty in the GM prediction of the SSH variance spectrum, we derive an independent estimate of the contribution of the internal-wave continuum on the submesoscale SSH variance spectrum from mooring observations (section 4). Our estimate confirms that the internal-wave continuum will unlikely exceed SWOT's noise level substantially.

3. Balanced flow extrapolation based on existing altimetry

In this section, we determine the scale down to which SWOT should be expected to resolve balanced flow.
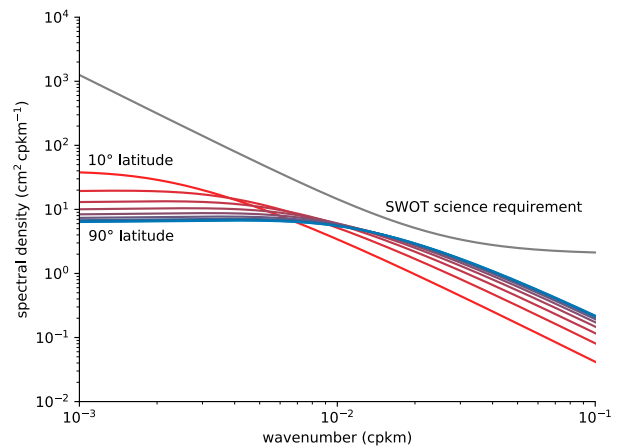

FIG. 2. GM prediction for the SSH variance spectrum of the internal-wave continuum. The curves are for standard parameters, the stratification is set it its surface value ($N = N_0$), and a range of inertial frequencies corresponding to 10° increments in latitude (red through blue lines). In all cases, the variance level of the internal-wave continuum is predicted to fall below SWOT's expected error spectrum (gray line).

The expected resolution scale depends on both the mesoscale energy level and the submesoscale roll-off of the SSH variance spectrum. The mesoscale energy level varies strongly from region to region, but it can be estimated with confidence from *Jason-2* along-track data. The submesoscale roll-off is more difficult to estimate from existing altimetry data because signals due to internal tides and measurement noise obscure the roll-off.

Xu and Fu (2011, 2012) diagnosed the submesoscale roll-off of SSH variance spectra from *Jason-1* and *Jason-2* data. They found large regional variations in the diagnosed spectral slope, but they did not distinguish between balanced flow and internal tides. The gentle roll-off they diagnosed in low-energy regions is most likely due to internal tides dominating the signal at small scales (Richman et al. 2012). We here instead assume, motivated by in situ observations and models, that the spectrum of the balanced flow follows a known power law of either k^{-4} or k^{-5} (section 2a).

The assumed submesoscale power laws should be appropriate everywhere except in the deep tropics, where the dynamics are dominated by equatorial waves. For simplicity, we nevertheless apply the same submesoscale power laws everywhere in the following analysis. Our results in the deep tropics should be met with some skepticism.

To determine the energy level of the balanced flow from *Jason-2* data, we must distinguish the SSH signal due to balanced flow from that due to internal tides and

measurement noise. We isolate the internal tide by taking advantage of its appearance as distinct peaks around the wavenumbers k_1 and k_2, which can independently be calculated from hydrography. We isolate the measurement noise by assuming it has a white spectrum.

We fit a model spectrum to wavenumber spectra obtained from *Jason-2* along-track data:

$$S(k) = \mathcal{B}(k) + \mathcal{T}_1(k) + \mathcal{T}_2(k) + \mathcal{N}. \tag{11}$$

This model spectrum consists of a balanced component $\mathcal{B}(k)$, components due to the first two modes of the semidiurnal internal tide $\mathcal{T}_1(k)$ and $\mathcal{T}_2(k)$, and a white noise level $\mathcal{N}$. Such a decomposition assumes that these four components are uncorrelated, which appears to be a reasonable leading-order description of the signal. We do not attempt to fit any signals due to the diurnal tide because we did not find any peaks at its modal wavenumbers except in one single region (centered on 8°S, 52°E). Our model spectrum also does not include any contribution from the internal-wave continuum because the SSH signature of the continuum is most likely too weak to contribute significantly to the *Jason-2* signal (see sections 2c and 4).

The balanced component is given the functional form

$$\mathcal{B}(k) = \frac{a_0}{1 + (k/k_0)^s}, \tag{12}$$

where a_0 sets the large-scale spectral level and k_0 determines at what wavenumber the spectrum transitions to a power law k^{-s}. The slope s is set to either $s = 4$ or $s = 5$. The functional form of (12) is chosen heuristically and allows for accurate fits to the data across the global ocean.

The tidal peaks are assumed to have a Gaussian shape around the independently calculated k_i, with amplitude a_i and width Δ_i:

$$\mathcal{T}_i(k) = a_i \exp\left[-\frac{(k - k_i)^2}{2\Delta_i^2} \right]. \tag{13}$$

The widths Δ_i are limited to below 2×10^{-3} cpkm to avoid very broad peaks that would improve the fit by capturing some of the signal that is clearly nontidal. This tidal model is motivated mainly by its ability to capture the tidal signals apparent in the data. The model assumes that internal tides project onto the altimetry tracks at wavenumbers close to the modal wavenumber. The width of the peaks is most likely the result of averaging over waves that propagate at various angles to the (ascending and descending) tracks.

The noise level $\mathcal{N}$ is simply a constant, representing white measurement noise. As the measurement noise varies regionally and seasonally, primarily because of variations in significant wave height (e.g., Zanifé et al. 2003), we determine it as part of our fit. We restrict ourselves to 1-Hz data and thus disregard the nonwhite noise structure at the higher wavenumbers accessible with 20-Hz data (e.g., Dibarboure et al. 2014).

SSH variance spectra are calculated from *Jason-2* data for every 8° × 8° region of the global ocean that has sufficient data. We use *Jason-2* along-track sea level anomaly data from 2008 to 2016 (https://data.nodc.noaa.gov/jason2/gdr/gdr_ssha), from which the barotropic tide has been removed. For every region, all ground tracks that cross the center longitude are considered, and data beyond the bounding latitudes are trimmed off. Every pass over these ground tracks is considered a segment. For every segment, the first 160 data points are selected; the remaining points are trimmed off. Only segments that have no missing data in these 160 data points are selected. For every segment satisfying these selection criteria, we remove the mean and linear trend from the SSH signal, apply a Hann window, and perform a discrete Fourier transform. The average spacing between data points is 5.87 km; we ignore variations in the spacing, which are less than 0.01 km. Spectra are calculated by averaging over all segments in a region. In a typical region, on the order of 500 segments enter the calculation, rendering the formal error of the spectral estimation very small. No spectra are calculated for regions with less than 100 segments.

For every 8° × 8° region, the seven parameters a_0, k_0, a_1, Δ_1, a_2, Δ_2, and $\mathcal{N}$ are determined using a least squares fit of the model spectrum $S(k)$ to the observed spectrum. Each term in the cost function is normalized by the square of the observed spectrum, a normalization that is required to sufficiently constrain the fit at high wavenumbers, where the spectral levels tend to be several orders of magnitude lower than at low wavenumbers. Separate fits are performed for $s = 4$ and $s = 5$.

We illustrate these fits with two regions that exhibit different dynamical regimes (Fig. 3). The region southwest of Hawaii shows all elements of our model spectrum: balanced flow at large scales, internal tides with discernible peaks at both the first- and second-mode wavenumbers, and a white-noise floor at small scales (Figs. 3a,c). This is a region with particularly strong internal tides—there even is a hint of a third mode (which we ignore for the fit because it is rare elsewhere in the global ocean). The full fit yields excellent agreement with the data.

In the Southern Ocean just southwest of Cape Agulhas, in contrast, internal tides are relatively weak (Figs. 3b,d). The balanced and white-noise components
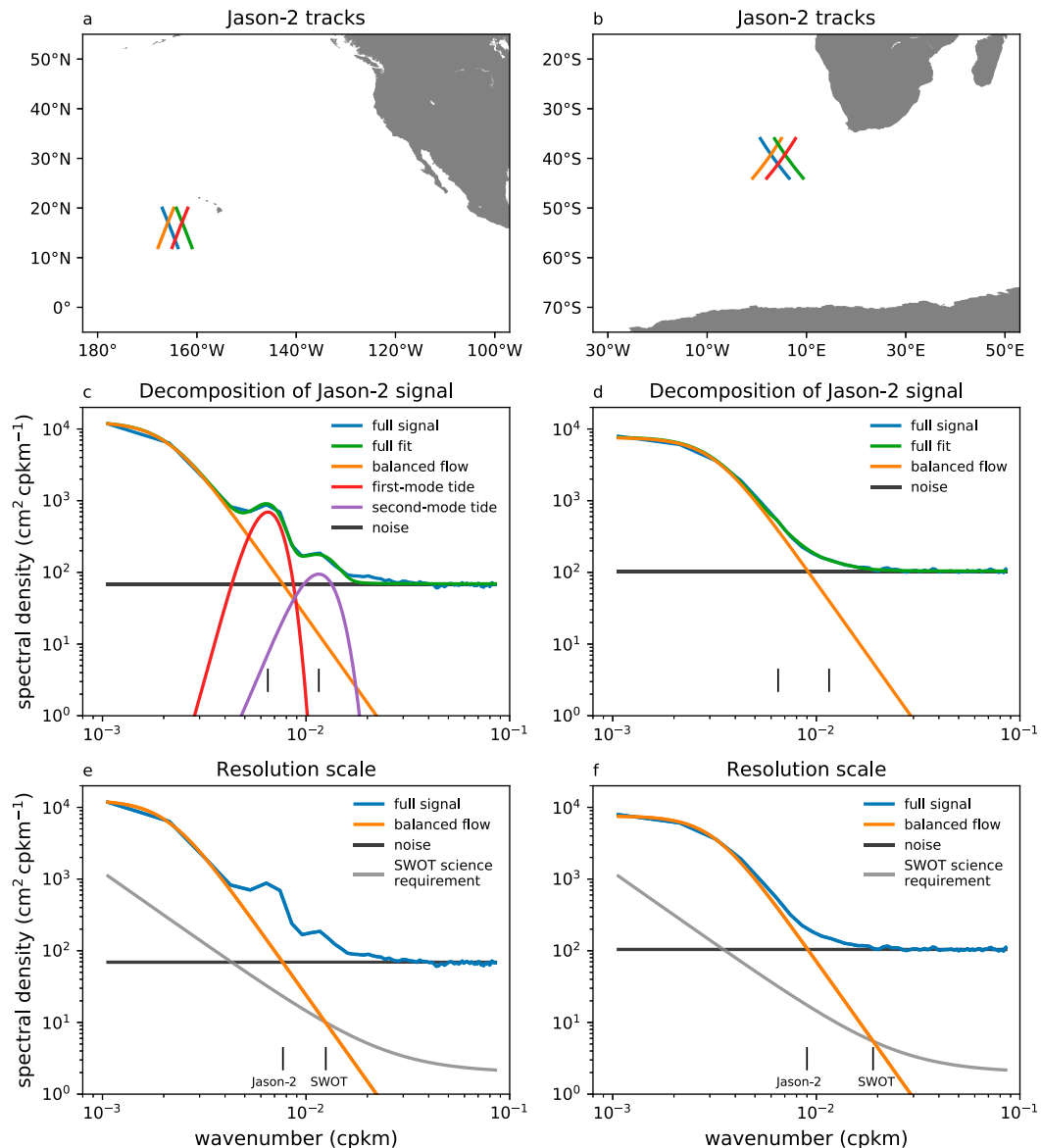
FIG. 3. Estimating SWOT's resolution scale by extrapolating the balanced component of *Jason-2* spectra to small scales. (a),(b) The *Jason-2* tracks (colored lines) used in two example regions. (c),(d) Decomposition of the full *Jason-2* SSH variance spectrum from the two example regions (blue lines), the balanced components (orange lines), the tidal components (red and purple lines), the noise components (black lines), and the full fits (green lines). The wavenumbers of the first two modes of the semidiurnal tide are computed from hydrography (black vertical lines). (e),(f) Using the balanced component of the SSH variance spectrum to extrapolate it to submesoscales given the fixed slope $s = 4$ of the strong submesoscales regime. The resolution scales (black vertical lines) are determined by the intersections with the *Jason-2* noise (black horizontal lines) and SWOT's expected error spectrum (gray lines).

are sufficient to match the observed spectrum with our model spectrum. We apply the same fitting procedure, however, which is robust enough to simply attribute negligible variance to the internal tide (not shown).

Our model spectrum yields a reasonable fit across the global ocean (Fig. 4). We quantify the misfit with the root-mean-square difference between the model spectrum and the observed spectrum, with the difference

normalized by the observed spectral density at the respective wavenumber (same as in the fit itself). The fit is generally better in the extratropics than in the tropics, which is not surprising given that we constructed the model spectrum based on expectations for the extratropics. In some tropical regions, the observed spectra exhibit a broadband small-scale signal that is slightly red and cannot be fit by our model (not shown). The maximum
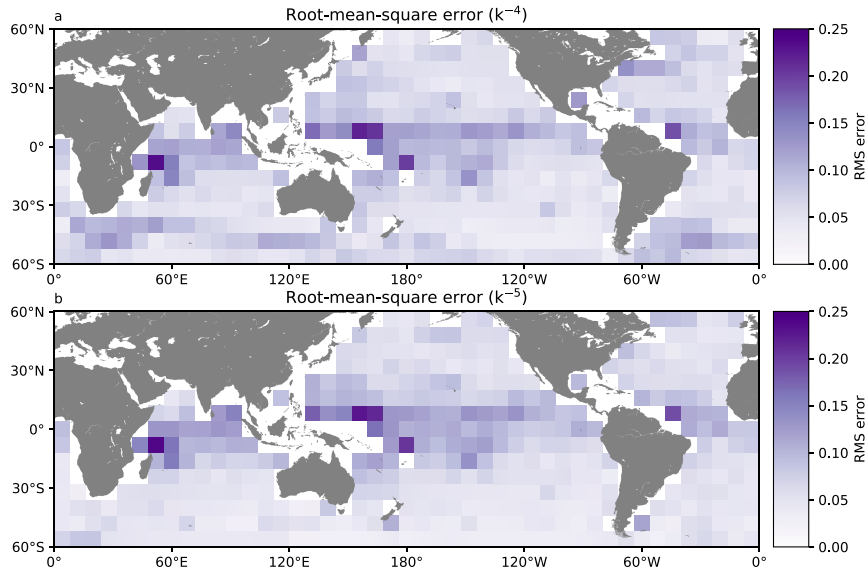
FIG. 4. Misfit between the model spectrum and the observed spectrum. (a),(b) Root-mean-square differences for the strong submesoscales regime ($s = 4$) and the weak submesoscales regime ($s = 5$). All differences are normalized by the spectral density of the observed spectrum.

misfit is still only 0.23, suggesting our model spectrum is overall appropriate.

The misfits also indicate that the observed spectra can be fit slightly more accurately with $s = 5$ than $s = 4$ (Fig. 4). This suggests that the observed spectra, which represent averages over all months of the year, are dominated by the weak submesoscales regime. More broadly, this suggests that the data do contain some useful information on the spectral slope of balanced flow, despite the small range of scales over which this slope is exhibited (Fig. 3d). We hope to report in the future the results of an ongoing analysis of the recoverable spectral slope and its seasonal variations.

With these fits, we are now in the position to determine SWOT's expected resolution scale for balanced flow. With a_0 and k_0 determined from the fit in each $8° \times 8°$ region and for both $s = 4$ and $s = 5$, we can calculate the wavelength at which the spectrum of the balanced flow $\mathcal{B}(k)$ intersects the error variance spectrum $R(k)$ given in (10).

For our calculation of the resolution scale of balanced flow, we disregard all signals due to internal tides. In reality, these will obscure the balanced flow at submesoscales and have to be removed to reveal the balanced flow in isolation (e.g., Fig. 3c). In effect, we pretend for the purpose of this analysis that these tidal signals can be removed perfectly—a task that is, of course, far from trivial.

Also note that our definition of the resolution scale as the intersection of the signal spectrum with the error

spectrum is relatively generous. It corresponds to a signal-to-noise ratio of one at the resolution scale. For many applications, a much higher signal-to-noise ratio may be required.

The resulting resolution scale of balanced flow exhibits strong regional variations (Figs. 5a,b). As expected, the estimated resolution is best in regions with strong mesoscale eddies, such as the Kuroshio region, the Gulf Stream region, and the Southern Ocean. High mesoscale energy entails strong submesoscale balanced flow, and a strong submesoscale signal implies improved resolution. In these high-energy regions, the resolution scale reaches a minimum of 24 km under the assumption of a strong submesoscales regime ($s = 4$), and a minimum of 35 km under the assumption of a weak submesoscales regime ($s = 5$). In regions with weak mesoscale eddies, for example, in the "eddy desert" of the eastern subpolar North Pacific, the resolution scale increases to order 100 km. The median extratropical (poleward of $20°$ latitude) resolution scale is 51 km for $s = 4$ and 74 km for $s = 5$.

There is a general deterioration in expected resolution toward the equator. In the tropics, our analysis yields resolution scales that are almost everywhere in excess of 100 km. The balanced flow, as determined by our fit to the observed spectra, is particularly weak here. It should be kept in mind, however, that our arguments based on in situ observations and numerical simulations of geostrophic turbulence likely break down in the deep tropics, that is, within a few degrees of the equator,
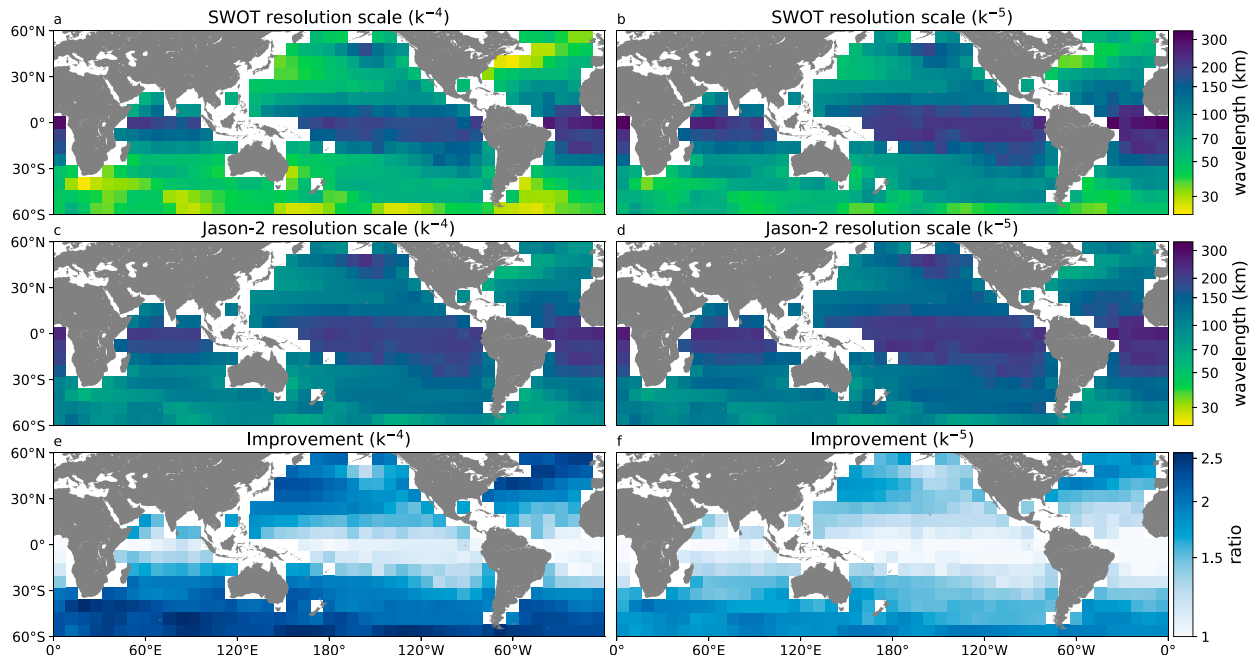
FIG. 5. Global estimates of SWOT's resolution scale for the balanced flow. (a),(b) SWOT's resolution scale for the strong submesoscales regime ($s = 4$) and the weak submesoscales regime ($s = 5$). (c),(d) *Jason-2*'s resolution scale for the same two regimes. (e),(f) Ratio between the resolution scales of SWOT and *Jason-2*.

where SSH signals tend to be dominated by equatorial waves. The submesoscale spectral roll-off there is much less well constrained. That said, the observed spectra in the tropics are still reasonably fit by our model spectrum. Much of the tropical submesoscale signal is accounted for by internal tides.

We compare the resolution scale expected for SWOT with that of *Jason-2*. The resolution scale of *Jason-2* is determined analogously by calculating the wavelength at which the balanced spectrum $\mathcal{B}(k)$ intersects the white noise floor $\mathcal{N}$ (Figs. 3e,f). The resulting *Jason-2* resolution scale is on the order of 100 km everywhere, with somewhat lower values in high-energy regions (Figs. 5c,d). The *Jason-2* resolution scale does not depend strongly on whether we set $s = 4$ or $s = 5$ because the intersection with the noise is closer to the mesoscale eddy scale k_0 than in the case of SWOT.[2]

This analysis suggests that the resolution scale should be expected to improve from *Jason-2* to SWOT by at most a factor of 2.6 (Fig. 5e). This maximal improvement occurs in high-energy regions and under the assumptions of the strong submesoscales regime. This is consistent with the scaling argument presented above, which predicts an improvement of $50^{1/4} = 2.7$. The scaling provides an upper bound on the improvement because it is based on white noise floors. The red-noise component of SWOT's error spectrum significantly deteriorates the expected resolution in many regions (e.g., Figs. 3e,f)—the extrapolated balanced spectrum intersects SWOT's error spectrum in the white-noise-dominated part in high-energy regions only. In the weak submesoscales regime, the maximal improvement in resolution scale is by a factor of 2.0 (Fig. 5f), as expected from $50^{1/5} = 2.2$.

We should note that we assume SWOT's error spectrum to be independent of space and time and of the signal itself. We ignore expected modulations of the white noise floor by the sea state, which gives rise to regional and seasonal variations (e.g., Wang et al. 2019). Taking these into account would have only minor effects on our analysis, however, because the balanced signal falls off so steeply: a factor of 2 reduction or increase in the noise floor would lead to a change of the resolution scale by a factor of at most $2^{1/4} = 1.19$ for $s = 4$ and $2^{1/5} = 1.15$ for $s = 5$.

Similarly, it is possible that SWOT's performance will exceed the science requirement defined by (10). But even a significant performance improvement, for

---

[2] Our calculation of *Jason-2*'s resolution scale ignores any noise that is correlated along the track (similar to the red-noise part of SWOT's expected error spectrum). In the tropics, where the signal is weak, this leads to an overestimation of *Jason-2*'s resolution, which in turn leads to an apparent deterioration in the resolution going to SWOT. This is, of course, impossible because the SWOT spacecraft will carry a Jason-class nadir altimeter in addition to the wide-swath interferometer.
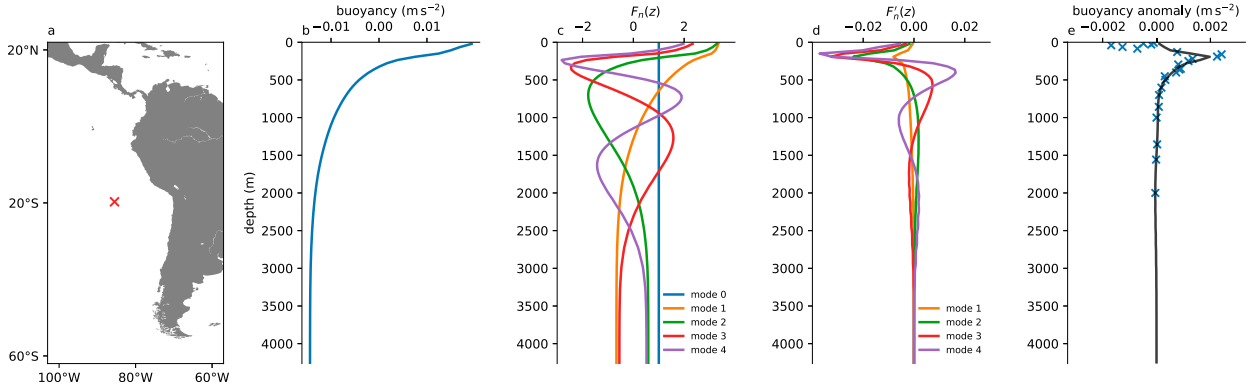
FIG. 6. Calculating the amplitudes of vertical modes from the Stratus XI mooring in the South Pacific. (a) The location of the mooring. (b) Mean buoyancy profile at the mooring location from the ECCO climatology. (c) The first five pressure modes F_n. (d) The first four buoyancy modes F'_n. (e) An example of the least squares fit of the observed buoyancy anomalies (blue crosses) with the first five buoyancy modes (black line).

example, a noise floor lowered by a factor of 2, would lead to only a modest improvement in the resolution of balanced flow.

We should also note that the SWOT science requirement is defined for SSH averages over 7.5 km ×7.5 km squares along the satellite's swath. Cross-track averaging reduces the noise level of the one-dimensional along-track spectrum and can thus improve the along-track resolution. Averaging instead over 15 km × 15 km squares, for example, would reduce the noise floor by a factor of 2 and improve the resolution by a factor of at most 1.19. Averaging over even larger squares may be feasible in some regions, but care must be taken to avoid attenuation of the resolvable signal. See Chelton et al. (2019) for a detailed discussion of this point.

4. Internal-wave continuum estimate from a mooring

We now turn to estimating the contribution that internal waves make to the wavenumber spectrum of SSH variance. The SSH signature of the internal-wave continuum is expected to be relatively uniform across the global ocean, so our estimate from a single mooring gives some guidance for the global signal (cf. Fig. 2). We focus on the internal-wave continuum, but our estimate includes the entire internal-wave field, and we use the signal from the internal tide to cross-check our estimate with existing *Jason-2* data.

Our approach is as follows: we use the temperature and salinity data from a mooring in the eastern subtropical South Pacific (Fig. 6a) to obtain time series of buoyancy anomalies at a range of depths that span the thermocline. We then use these data to estimate the amplitudes of the first five vertical modes of buoyancy (cf. Wunsch 1997). From these buoyancy modes,

we calculate the pressure modes and their surface signature to infer the SSH signal. We calculate modal frequency spectra, which we subsequently turn into horizontal wavenumber spectra using linear theory.

We use data from the Stratus XI mooring (deployed 6 April 2011 to 29 May 2012), which has good vertical coverage of MicroCAT instruments that measure temperature and salinity at high temporal resolution (5 min). The vertical coverage is crucial for the modal estimation described below. For each of the 27 instruments, we calculate the potential density ρ (referenced to 2000 m) using the TEOS-10 seawater toolbox (McDougall and Barker 2011) and calculate buoyancy as $B = -g(\rho - \rho_0)/\rho_0$, where g is the gravitational acceleration, and $\rho_0 = 1035\,\mathrm{kg\,m^{-3}}$ is a constant reference density (the average potential density of the full dataset). From each instrument's time series of buoyancy, we subtract the time mean to obtain the buoyancy anomalies b that we then use to estimate the modal amplitudes.

Pressure and buoyancy anomalies can be decomposed into vertical modes as follows:

$$p(x,y,z,t) = \sum_{n=1}^{\infty} F_n(z) p_n(x,y,t), \tag{14}$$

$$b(x,y,z,t) = \sum_{n=1}^{\infty} F'_n(z) b_n(x,y,t), \tag{15}$$

where it should be noted that F'_n has units of inverse length, so the b_n do not have the same units as b. We calculate the modes F_n and F'_n from the ECCO climatology (appendix B). Projecting the hydrostatic relation $b = \rho_0^{-1} \partial p/\partial z$ onto F'_n/N^2 yields that $b_n = p_n/\rho_0$, so we can estimate the modal coefficients of pressure p_n by estimating the modal coefficients of buoyancy b_n from the data.

In principle, the modal coefficients can be calculated by projecting a full profile of buoyancy anomalies onto the orthogonal modes. Since we have buoyancy anomalies at 27 depths only, however, such a projection is not feasible. One could perfectly match the data at the 27 depths with 27 modes, but such a calculation is hopelessly ill-conditioned and dramatically overestimates the modal amplitudes. We thus resort to a least squares fit to estimate the first five modes only. In the fit, we weight the instruments by their distance to neighboring instruments. Experimentation with synthetic and model data suggests we can make this estimation from the Stratus instruments with confidence. The first five modes are sufficient to capture the vast majority of the total variance. Our results are insensitive to the number of modes included as long as that number is greater than or equal to 4, such that the majority of the SSH variance can be captured, and smaller than 10, such that the fit is well conditioned (Fig. 6).[3]

The fits give us time series of the modal coefficients b_n for $n = 1, \ldots, 5$. From these, we can calculate the modal contributions to surface pressure and thus SSH as $h_n = p_n F_n(0)/\rho_0 g$. We compute frequency spectra by applying Hann windows to the time series, performing Fourier transforms, and averaging the resulting spectrograms over 20 frequency bins per decade that are equally spaced in log space.

While the orthogonality of the modes F_n ensures that quantities like the vertically integrated energy diagonalize, that is, that these quantities can be written as sums over the variances contributed by each mode, it does not guarantee that the same is true for the SSH variance. Only if the modal coefficients are uncorrelated is the frequency spectrum of SSH variance equal to the sum of the frequency spectra of the modal contributions, whereas in general

$$S(\omega) = \left| \sum_{n=1}^{\infty} \hat{h}_n(\omega) \right|^2 \neq \sum_{n=1}^{\infty} |\hat{h}_n(\omega)|^2. \tag{16}$$

Luckily, the data suggest that the modal coefficients *are* largely uncorrelated (Fig. 7a). The SSH variance spectrum is to leading order matched by the sum over the modes, especially in the internal-wave band. It is this observation of a lack of mode correlation that makes it meaningful to talk about modal contributions to the

SSH variance and, crucially, allows us to convert modal frequency spectra to wavenumber space.

Note that the sum over the modes slightly overestimates the SSH variance spectrum, which might suggest that our estimate should be taken as an upper bound on the true contribution of internal waves to the wavenumber spectrum of SSH variance. It is unclear, however, how modal correlations propagate through our conversion from frequency to wavenumber space. Further note that the overestimation is most pronounced in the inertial and slightly subinertial frequency band, probably because these frequencies are dominated by surface-trapped flows that project onto a number of vertical modes and thereby create mode correlation. This frequency band does not affect the estimation of the SSH signal due to the internal-wave continuum.

The total frequency spectrum of SSH variance is strongly dominated by the first two modes (Fig. 7a). The variance contained in higher modes decreases rapidly with mode number. As expected, there is a broadband signal at subinertial frequencies, a prominent semidiurnal peak, a less prominent diurnal peak, and an inertial peak of similar magnitude.[4] The internal-wave continuum occupies the frequency range between the inertial frequency and 2×10^{-4} cps, with its broadband nature punctuated by the peaks. There are some suspicious bumps at frequencies larger than 2×10^{-4} cps, where nonhydrostatic effects may come into play. This high-frequency signal should be interpreted with caution but does not affect our main results.

We convert the superinertial part of the modal spectra into wavenumber spectra using the modal dispersion relation. The conversion factor is $d\omega/d\kappa = c_n^2 \kappa/\omega$, and the dispersion relation (3) relates the frequency ω to the wavenumber magnitude κ. Assuming horizontal isotropy, we then estimate the one-dimensional wavenumber spectra using

$$S_n(k) = \frac{2}{\pi} \int_k^{\infty} \frac{S_n(\kappa)\, d\kappa}{(\kappa^2 - k^2)^{1/2}}, \tag{17}$$

with the upper limit of the integration in practice given by the wavenumber corresponding to the Nyquist frequency. This conversion preserves the ordering of the modal contributions (Fig. 7b), except that the semidiurnal peak of the second mode now sticks out over the continuum contribution of the first mode.

---

[3] The procedure could probably be made more robust by assigning a priori variances to the modes that decay with mode number (cf. Wunsch 1997). Our analysis of SSH variance spectra, however, requires the amplitudes of the first few modes only, for which our simple least squares procedure is sufficient.

[4] The occurrence of an inertial peak in buoyancy (or temperature) variance spectra is not uncommon and typically attributed to either horizontal advection or mooring motion (e.g., Fu 1981). The inertial signal is suppressed in the conversion to SSH, so it does not affect our estimate of SSH variance.
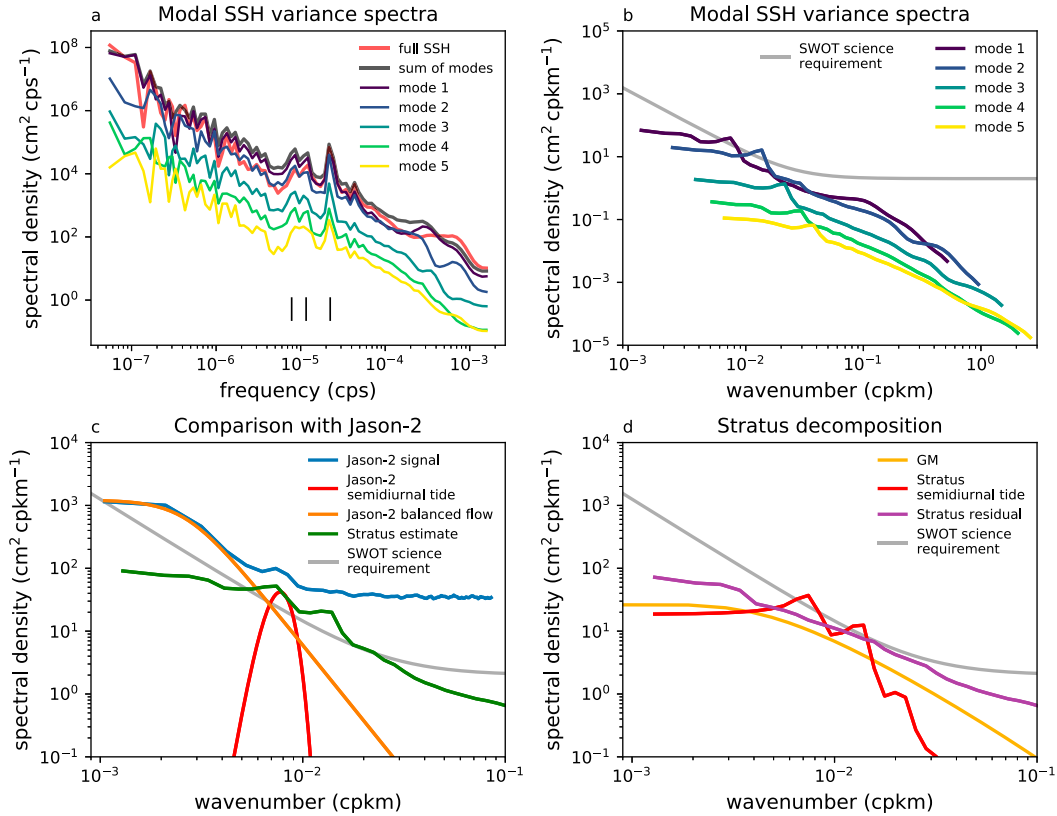
FIG. 7. Estimating the SSH variance due to internal waves from mooring observations. (a) Frequency spectra of SSH variance, as estimated from the modal fits to the buoyancy data from the mooring. Shown are the frequency spectrum of the full SSH variance (red line), the sum of the SSH variance spectra of the modes (black line), and the SSH variance spectra of the individual modes (colored lines). The black vertical lines show the inertial frequency, the frequency of the diurnal tide, and the frequency of the semidiurnal tide. (b) One-dimensional wavenumber spectra of SSH variance converted from the modal frequency spectra (colored lines) and comparison to SWOT's expected error spectrum (gray line). (c) Comparison of the total spectrum estimated from the mooring (summed over all modes, green line) with SWOT's expected error spectrum (gray line) and with the *Jason-2* spectrum (blue line) and its decomposition into balanced flow (orange line) and the first-mode semidiurnal tide (red line). (d) Decomposition of the mooring estimate into contributions from the semidiurnal tide (red line) and the rest of the internal-wave band (purple line). The estimates are compared to the Garrett–Munk spectrum (yellow line) and SWOT's expected error spectrum (gray line).

The sum of these modal wavenumber spectra provides an estimate of the full signal of internal waves at the sea surface in the submesoscale range (Fig. 7c). The SSH signal due to internal waves falls off much more gently than the expectation for the balanced flow. This means that internal waves start strongly dominating the SSH signal at small scales. In this location, the transition from a signal dominated by balanced flow to one dominated by internal waves occurs around 200 km and is already resolved by *Jason-2*. The additional signal accessible by SWOT should be dominated entirely by internal waves.

The Stratus region is one with relatively weak balanced flows, and the transition from a signal dominated by balanced flow to one dominated by waves should occur at much smaller scales in high-energy regions

(cf. Qiu et al. 2018). This transition is inevitable, however, because the internal-wave signal falls off much less steeply than the balanced signal.

As a check on the accuracy of our conversion, we compare our estimate with the SSH variance spectrum from *Jason-2* (Fig. 7c). We use an $8° \times 8°$ region centered on the Stratus mooring and apply the same decomposition into balanced, tidal, and noise components as in the previous section. The tidal component estimated from *Jason-2* data matches the converted internal-wave spectrum from the mooring. The rest of the internal-wave signal is drowned out by the noise in the *Jason-2* data, but the match at the mode-1 tidal peak increases our confidence in the estimate at higher wavenumbers as well.

For the Stratus region, the part of the internal-wave signal that rises significantly above SWOT's expected error spectrum is dominated by the first two modes of the semidiurnal tide (Fig. 7c). As our estimate of the internal-wave signal originates in frequency space, we can explicitly decompose it into a semidiurnal and a residual component. We linearly interpolate the spectrum between the frequencies 1.9×10^{-5} cps and 2.7×10^{-5} cps that bracket the semidiurnal peak, and we attribute the variance above the interpolation to the semidiurnal tide. The residual, consisting of the signal outside of the semidiurnal band and the linear interpolation across the semidiurnal band, contains the internal-wave continuum as well as minor contributions from both the diurnal tide and a small peak at twice the semidiurnal frequency (presumably a tidal harmonic).

In wavenumber space, this residual component falls slightly below SWOT's expected error spectrum (Fig. 7d). This suggests that the internal-wave continuum may be detectable in SWOT data, but it will be a challenge to distinguish it from the noise. The GM spectrum, calculated with standard parameters (except that we set $f = 5 \times 10^{-5}$ s^{-1} and $N = 7 \times 10^{-3}$ s^{-1}) is roughly consistent with our mooring-based residual spectrum but consistently somewhat lower. One should not expect an exact match, but part of the mismatch may be due to tidal contributions to our residual spectrum. The general consistency increases our confidence both in our mooring-based estimate and in the GM estimate of the SSH signal.

5. Comparison to previous estimates

Previous studies have estimated SWOT's resolution scale to be around 15 km (Fu and Ferrari 2008; Fu and Ubelmann 2014; Desai et al. 2018). These estimates relied on extrapolating the globally averaged SSH variance spectrum from nadir altimetry to small scales, using a slope of around $s = 2$ that was estimated from the high-wavenumber end of the observed spectrum.

We obtained larger values for the resolution scale in section 3 because we distinguished between balanced flow and internal waves. The globally averaged SSH variance spectrum used previously includes sizable contributions from internal tides, which in a global average do not appear as distinct peaks anymore. The tidal contributions flatten out the spectrum and thus reduce the slope used for extrapolation. An SSH variance spectrum as flat as k^{-2} is unrealistic for balanced flow, so the previous estimate of 15 km—if interpreted as an estimate for balanced flow—is unrealistically small.

In many regions, SWOT's full signal at the smallest resolvable scales will be dominated by internal tides.

This means that the resolution of the full signal is determined by the strength of the internal tide. The example from the Stratus mooring suggests that SWOT will resolve the second mode semidiurnal tide there, with an expected resolution scale of about 50 km. The resolution of higher modes appears possible in regions with stronger internal tides.

Recently, SWOT's resolution was also assessed using high-resolution numerical models. Wang et al. (2019) gave regional and seasonal estimates of SWOT's resolution scale: about 15 km in low latitudes and 30–45 km in midlatitudes. In their resolution estimates, however, they did not distinguish between balanced flow and internal waves. Their estimates should thus be compared to our estimates for the balanced flow in high-energy regions only, where internal-wave contributions to the 10–100-km signal are negligible. In these regions, the two estimates are roughly consistent.

Chelton et al. (2019) performed an extensive analysis of the mapping capabilities of SWOT and a prospective Winds and Currents Mission. Their analysis was based largely on a regional simulation of the California Current System that did not include high-frequency forcing and is thus dominated by balanced flow. Their estimate for SWOT's in-swath resolution of geostrophic velocities is about 50 km, which is consistent with our estimate for the resolution scale of the balanced flow in that region (Fig. 5).

6. Conclusions

The main conclusion of this study is that it is exceedingly challenging to measure the SSH field with high-enough accuracy to infer submesoscale balanced flow. Even if submesoscale balanced flow is energetic, its SSH variance spectrum falls off like k^{-4}, which implies that an increase in resolution by one order of magnitude requires a decrease in the noise level by *four* orders of magnitude. This means that the resolution increase from SWOT, resulting from a 50-fold reduction in the noise level, should be expected to be relatively modest.

Extrapolating SSH variance spectra calculated from *Jason-2* data, we obtain a SWOT resolution scale for balanced flow of about 30 km in regions with high eddy activity, such as western boundary regions and the Southern Ocean, and a much coarser resolution in regions with weaker eddy activity. Compared to *Jason-2*, the resolution scale is estimated to increase by typically less than a factor of 2—with the exception of high-energy regions with energetic submesoscales, where the resolution is estimated to increase by up to a factor of 2.6.

The rapid drop-off of the SSH variance spectrum of balanced flow contrasts with the signal contributed by internal waves. Low-mode internal tides, which in many regions already dominate *Jason-2* data near its resolution scale, should be expected to be a prominent part of SWOT's submesoscale signal.

The SSH signal due to the internal-wave continuum is predicted to fall off like k^{-2} (in the hydrostatic limit of GM), suggesting a transition from balanced to wave-dominated signals at submesoscales. This transition is similar to what has been observed in kinetic-energy spectra in the ocean's interior (Callies and Ferrari 2013; Bühler et al. 2014; Callies et al. 2015; Rocha et al. 2016a; Qiu et al. 2017), but the transition should be more abrupt in SSH variance because the spectral slopes of the two flow components differ more dramatically (cf. Qiu et al. 2018). Our estimates suggest, however, that the transition to an SSH signal dominated by the internal-wave continuum will be difficult to observe with SWOT. We estimate the variance level of the internal-wave continuum to lie somewhat below SWOT's expected error spectrum.

As any new measurements, SWOT data may present us with surprises. Only after launch will we find out what the SSH signals truly look like in the submesoscale range. We hope, nevertheless, that the expectations outlined in this study will help interpret the data once SWOT is in orbit.

APPENDIX A

Shipboard ADCP Data

We calculate the variance spectrum of cross-track velocities from shipboard ADCP data retrieved from the Joint Archive for shipboard ADCP (http://ilikai.soest.hawaii.edu/sadcp/). The data was collected during the 1996 R/V *Knorr* cruise KN9611 in the eastern North Atlantic (Fig. 1). We break the data into 16 legs between stations, fit a straight line to each leg, and rotate the velocities into the along-track coordinate systems defined by these lines. We remove each leg's mean velocity, apply a Hann window, and perform a Fourier transform. We average the resulting spectrograms over all legs and 10 wavenumber bins logarithmically spaced between 10^{-3} and 10^{-1} cpkm.

APPENDIX B

Calculation of Vertical Modes

We compute the vertical modes from the ECCO version 4 interpolated climatology (Forget et al. 2015; http://www.ecco-group.org/products.htm). For every 1° grid point, we average the potential temperature and salinity profiles over all months, compute potential density ρ (referenced to 2000 m) using the TEOS-10 seawater toolbox (McDougall and Barker 2011), and thus obtain the buoyancy $B = -g(\rho - \rho_0)/\rho_0$ with ρ_0 here being the depth-average potential density. We plug the buoyancy into a finite-difference version of (2) with $N^2 = dB/dz$ and solve the resulting matrix equation for its eigenvectors F_n and eigenvalues $-1/c_n^2$. We normalize the modes such that

$$\frac{1}{H}\int_{-H}^{0} F_n F_m \, dz = \delta_{nm}, \tag{18}$$

where δ_{nm} is the Kronecker delta. For every $8° \times 8°$ region used in the resolution analysis, we pick the median eigenvalue as representative of the region, and we obtain the modal wavenumbers of the semidiurnal internal tide using the dispersion relation (3). The global variations are consistent with Chelton et al.'s (1998) maps (Fig. B1). To calculate the modes for the Stratus mooring (section 4), we use the closest ECCO grid point.

Similarly, we calculate the modes F_n' by solving the eigenvalue problem resulting from the finite difference version of

$$\frac{d^2}{dz^2}\left(\frac{1}{N^2}F'\right) + \frac{1}{c^2}F' = 0,$$
$$F' = 0 \quad \text{at} \quad z = 0 \quad \text{and} \quad z = -H. \tag{19}$$

The resulting modes satisfy the orthogonality condition

$$\frac{1}{H}\int_{-H}^{0}\frac{1}{N^2}F_n'F_m' \, dz = \frac{\delta_{nm}}{c_n^2}. \tag{20}$$

APPENDIX C

Global Structure of Tidal SSH Signatures

The global structure of SSH variance associated with internal tides is quite different from that of kinetic energy. This is because the conversion from kinetic energy to SSH variance depends strongly on the ratio of the tidal frequency to the local inertial frequency and on the local phase speed c_n (cf. Qiu et al. 2018).
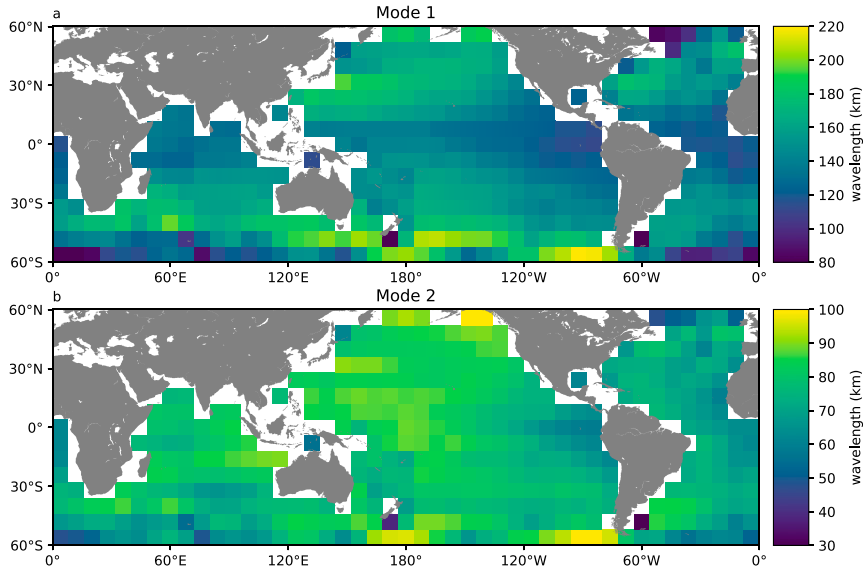
FIG. B1. Wavelengths of the first two vertical modes of the semidiurnal internal tide. The estimates are computed from the ECCO climatology, and shown is the median value for every $8° \times 8°$ box.

The linear momentum equations for a modal plane wave are

$$-i\omega\hat{u}_n - f\hat{v}_n = -ikg\hat{h}_n, \tag{21}$$

$$-i\omega\hat{v}_n + f\hat{u}_n = -ilg\hat{h}_n, \tag{22}$$

where $\hat{h}_n = \hat{p}_n/\rho_0 g$ is the Fourier amplitude of SSH. Solving this for the two velocity components gives

$$\hat{u}_n = \frac{ifl + k\omega}{\omega^2 - f^2} g\hat{h}_n, \tag{23}$$

$$\hat{v}_n = \frac{-ifk + l\omega}{\omega^2 - f^2} g\hat{h}_n, \tag{24}$$

from which we obtain the kinetic energy

$$|\hat{u}_n|^2 + |\hat{v}_n|^2 = g^2 \frac{\omega^2 + f^2}{(\omega^2 - f^2)^2}(k^2 + l^2)|\hat{h}_n|^2. \tag{25}$$

Using the dispersion relation for hydrostatic internal waves in a flat-bottomed ocean (2), the SSH signal can be related to the surface kinetic energy by (for $\omega^2 > f^2$)
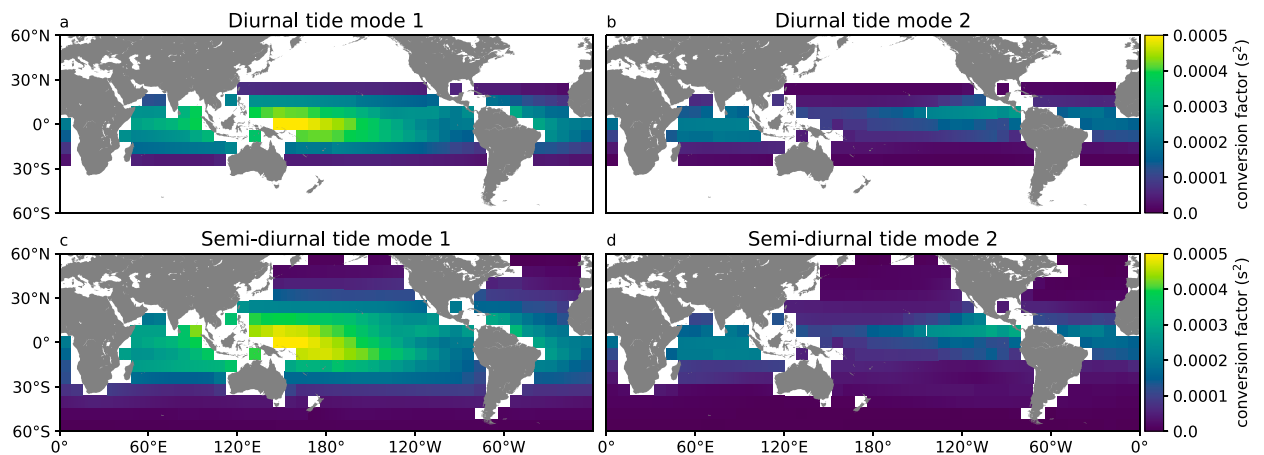

FIG. C1. Conversion factor from kinetic energy to SSH variance in (26). (a),(b) The conversion factor for the first two modes of the diurnal tide. We show the conversion factor only equatorward of the turning latitude. (c),(d) The conversion factor for the first two modes of the semidiurnal tide.

$$|\hat{h}_n|^2[F_n(0)]^2 = \frac{c_n^2}{g^2}\frac{\omega^2 - f^2}{\omega^2 + f^2}[F_n(0)]^2(|\hat{u}_n|^2 + |\hat{v}_n|^2). \qquad (26)$$

Note that the sum of this equation over all modes is the true SSH variance spectrum only if the modes are uncorrelated (see section 4). Available data suggest that this is a reasonable hypothesis, so we can talk about modal contributions to the total SSH variance.

It is instructive to assess the global structure of the conversion factor between SSH variance and kinetic energy in (26) (Fig. C1). The most striking feature is the poleward decay of the conversion factor toward the tides' turning latitudes. Since the turning latitude is much further poleward for semidiurnal than diurnal tides, the SSH signature of semidiurnal tides is expected to be much more prominent in much of the global ocean, even if diurnal tides have comparable kinetic energies. This is consistent with the *Jason-2* data, for which we found prominent peaks due to the semidiurnal tide, but almost no peaks due to the diurnal tide.

Changes in stratification introduce a zonal structure into the conversion factor in (26) (Fig. C1). Notably, this would suggest larger SSH amplitudes of first-mode tides in the western than in the eastern tropical Pacific—and the reverse for second-mode tides.

Poleward of their turning latitude, internal tides are evanescent. It is possible that they still contribute to the SSH signal near strong generation sites, but generally the signal is much weaker than equatorward of the turning latitude (e.g., Savage et al. 2017a).

The relation (26) also predicts the tidal SSH signals to decay with mode number, following the decay of c_n with mode number. For an exponentially decaying stratification and under the WKB approximation, $c_n \sim n^{-1}$, so the conversion factor alone predicts a decrease of the tidal-peak amplitude proportional to the square of the mode number. Since $\kappa_n \sim n$ (again under WKB scaling), the conversion factor predicts the tidal-peak amplitude to decay as κ_n^{-2}. The actual decay depends on the partitioning of kinetic energy between the modes and is likely more rapid than κ_n^{-2} because kinetic energy typically decays with mode number (see decay for $n > 2$ in Fig. 7b).

REFERENCES

Abernathey, R. P., and J. Marshall, 2013: Global surface eddy diffusivities derived from satellite altimetry. *J. Geophys. Res. Oceans*, **118**, 901–916, https://doi.org/10.1002/jgrc.20066.

Arbic, B. K., S. T. Garner, R. W. Hallberg, and H. L. Simmons, 2004: The accuracy of surface elevations in forward global barotropic and baroclinic tide models. *Deep-Sea Res. II*, **51**, 3069–3101, https://doi.org/10.1016/j.dsr2.2004.09.014.

Boccaletti, G., R. Ferrari, and B. Fox-Kemper, 2007: Mixed layer instabilities and restratification. *J. Phys. Oceanogr.*, **37**, 2228–2250, https://doi.org/10.1175/JPO3101.1.

Bühler, O., J. Callies, and R. Ferrari, 2014: Wave–vortex decomposition of one-dimensional ship-track data. *J. Fluid Mech.*, **756**, 1007–1026, https://doi.org/10.1017/jfm.2014.488.

Callies, J., and R. Ferrari, 2013: Interpreting energy and tracer spectra of upper-ocean turbulence in the submesoscale range (1–200 km). *J. Phys. Oceanogr.*, **43**, 2456–2474, https://doi.org/10.1175/JPO-D-13-063.1.

——, and ——, 2018: Baroclinic instability in the presence of convection. *J. Phys. Oceanogr.*, **48**, 45–60, https://doi.org/10.1175/JPO-D-17-0028.1.

——, ——, J. M. Klymak, and J. Gula, 2015: Seasonality in submesoscale turbulence. *Nat. Commun.*, **6**, 6862, https://doi.org/10.1038/ncomms7862.

——, G. Flierl, R. Ferrari, and B. Fox-Kemper, 2016: The role of mixed-layer instabilities in submesoscale turbulence. *J. Fluid Mech.*, **788**, 5–41, https://doi.org/10.1017/jfm.2015.700.

Capet, X., J. C. McWilliams, M. J. Molemaker, and A. F. Shchepetkin, 2008: Mesoscale to submesoscale transition in the California Current System. Part I: Flow structure, eddy flux, and observational tests. *J. Phys. Oceanogr.*, **38**, 29–43, https://doi.org/10.1175/2007JPO3671.1.

Charney, J. G., 1971: Geostrophic turbulence. *J. Atmos. Sci.*, **28**, 1087–1095, https://doi.org/10.1175/1520-0469(1971)028<1087:GT>2.0.CO;2.

Chavanne, C. P., and P. Klein, 2010: Can oceanic submesoscale processes be observed with satellite altimetry? *Geophys. Res. Lett.*, **37**, L22602, https://doi.org/10.1029/2010GL045057.

Chelton, D. B., R. A. deSzoeke, M. G. Schlax, K. E. Naggar, and N. Siwertz, 1998: Geographical variability of the first baroclinic Rossby radius of deformation. *J. Phys. Oceanogr.*, **28**, 433–460, https://doi.org/10.1175/1520-0485(1998)028<0433:GVOTFB>2.0.CO;2.

——, M. G. Schlax, and R. M. Samelson, 2011: Global observations of nonlinear mesoscale eddies. *Prog. Oceanogr.*, **91**, 167–216, https://doi.org/10.1016/j.pocean.2011.01.002.

——, ——, ——, J. T. Farrar, M. J. Molemaker, J. C. McWilliams, and J. Gula, 2019: Prospects for future satellite estimation of small-scale variability of ocean surface velocity and vorticity. *Prog. Oceanogr.*, **173**, 256–350, https://doi.org/10.1016/j.pocean.2018.10.012.

Desai, S., L.-L. Fu, S. Cherchali, and P. Vaze, 2018: Surface Water and Ocean Topography Mission (SWOT) Project science requirements document. Tech. Rep. JPL D-61923, Jet Propulsion Laboratory, California Institute of Technology, 29 pp., https://swot.jpl.nasa.gov/docs/D-61923_SRD_Rev_B_20181113.pdf.

Dibarboure, G., F. Boy, J. D. Desjonqueres, S. Labroue, Y. Lasne, N. Picot, J. C. Poisson, and P. Thibaut, 2014: Investigating short-wavelength correlated errors on low-resolution mode altimetry. *J. Atmos. Oceanic Technol.*, **31**, 1337–1362, https://doi.org/10.1175/JTECH-D-13-00081.1.

Dushaw, B. D., and P. F. Worcester, 1998: Resonant diurnal internal tides in the North Atlantic. *Geophys. Res. Lett.*, **25**, 2189–2192, https://doi.org/10.1029/98GL01583.

——, ——, and M. A. Dzieciuch, 2011: On the predictability of mode-1 internal tides. *Deep-Sea Res. I*, **58**, 677–698, https://doi.org/10.1016/j.dsr.2011.04.002.

Egbert, G. D., and R. D. Ray, 2000: Significant dissipation of tidal energy in the deep ocean inferred from satellite altimeter data. *Nature*, **405**, 775–778, https://doi.org/10.1038/35015531.

——, and ——, 2003: Semi-diurnal and diurnal tidal dissipation from TOPEX/Poseidon altimetry. *Geophys. Res. Lett.*, **30**, 1907, https://doi.org/10.1029/2003GL017676.

——, A. F. Bennett, and M. G. G. Foreman, 1994: TOPEX/POSEIDON tides estimated using a global inverse model. *J. Geophys. Res.*, **99**, 24 821, https://doi.org/10.1029/94JC01894.

Esteban Fernandez, D., L.-L. Fu, B. Pollard, and P. Vaze, 2017: SWOT Project mission performance and error budget. Tech. Rep., Jet Propulsion Laboratory, California Institute of Technology, 117 pp.

Ferrari, R., 2011: A frontal challenge for climate models. *Science*, **332**, 316–317, https://doi.org/10.1126/science.1203632.

——, and C. Wunsch, 2009: Ocean circulation kinetic energy: Reservoirs, sources, and sinks. *Annu. Rev. Fluid Mech.*, **41**, 253–282, https://doi.org/10.1146/annurev.fluid.40.111406.102139.

Forget, G., J. Campin, P. Heimbach, C. N. Hill, R. M. Ponte, and C. Wunsch, 2015: ECCO version 4: An integrated framework for non-linear inverse modeling and global ocean state estimation. *Geosci. Model Dev.*, **8**, 3071–3104, https://doi.org/10.5194/gmd-8-3071-2015.

Fox-Kemper, B., and R. Ferrari, 2008: Parameterization of mixed layer eddies. Part II: Prognosis and impact. *J. Phys. Oceanogr.*, **38**, 1166–1179, https://doi.org/10.1175/2007JPO3788.1.

——, and Coauthors, 2011: Parameterization of mixed layer eddies. III: Implementation and impact in global ocean climate simulations. *Ocean Modell.*, **39**, 61–78, https://doi.org/10.1016/j.ocemod.2010.09.002.

Fu, L.-L., 1981: Observations and models of inertial waves in the deep ocean. *Rev. Geophys.*, **19**, 141–170, https://doi.org/10.1029/RG019i001p00141.

——, and R. Ferrari, 2008: Observing oceanic submesoscale processes from space. *Eos, Trans. Amer. Geophys. Union*, **89**, 488–499, https://doi.org/10.1029/2008EO480003.

——, and C. Ubelmann, 2014: On the transition from profile altimeter to swath altimeter for observing global ocean surface topography. *J. Atmos. Oceanic Technol.*, **31**, 560–568, https://doi.org/10.1175/JTECH-D-13-00109.1.

Garrett, C., 1979: Mixing in the ocean interior. *Dyn. Atmos. Oceans*, **3**, 239–265, https://doi.org/10.1016/0377-0265(79)90011-3.

——, and W. H. Munk, 1972: Space-time scales of internal waves. *Geophys. Fluid Dyn.*, **3**, 225–264, https://doi.org/10.1080/03091927208236082.

——, and ——, 1975: Space-time scales of internal waves: A progress report. *J. Geophys. Res.*, **80**, 291–297, https://doi.org/10.1029/JC080i003p00291.

——, and ——, 1979: Internal waves in the ocean. *Annu. Rev. Fluid Mech.*, **11**, 339–369, https://doi.org/10.1146/annurev.fl.11.010179.002011.

——, and E. Kunze, 2007: Internal tide generation in the deep ocean. *Annu. Rev. Fluid Mech.*, **39**, 57–87, https://doi.org/10.1146/annurev.fluid.39.050905.110227.

Gill, A. E., 1982: *Atmosphere–Ocean Dynamics*. Academic Press, 662 pp.

Kantha, L. H., and C. C. Tierney, 1997: Global baroclinic tides. *Prog. Oceanogr.*, **40**, 163–178, https://doi.org/10.1016/S0079-6611(97)00028-1.

Kelly, S. M., 2016: The vertical mode decomposition of surface and internal tides in the presence of a free surface and arbitrary topography. *J. Phys. Oceanogr.*, **46**, 3777–3788, https://doi.org/10.1175/JPO-D-16-0131.1.

Klein, P., and G. Lapeyre, 2009: The oceanic vertical pump induced by mesoscale and submesoscale turbulence. *Annu. Rev. Mar. Sci.*, **1**, 351–375, https://doi.org/10.1146/annurev.marine.010908.163704.

Klymak, J. M., and J. N. Moum, 2007: Oceanic isopycnal slope spectra. Part II: Turbulence. *J. Phys. Oceanogr.*, **37**, 1232–1245, https://doi.org/10.1175/JPO3074.1.

Lapeyre, G., and P. Klein, 2006: Dynamics of the upper oceanic layers in terms of surface quasigeostrophy theory. *J. Phys. Oceanogr.*, **36**, 165–176, https://doi.org/10.1175/JPO2840.1.

Lévy, M., P. Klein, A.-M. Tréguier, D. Iovino, G. Madec, S. Masson, and K. Takahashi, 2010: Modifications of gyre circulation by sub-mesoscale physics. *Ocean Modell.*, **34**, 1–15, https://doi.org/10.1016/j.ocemod.2010.04.001.

——, D. Iovino, L. Resplandy, P. Klein, G. Madec, A.-M. Tréguier, S. Masson, and K. Takahashi, 2012: Large-scale impacts of submesoscale dynamics on phytoplankton: Local and remote effects. *Ocean Modell.*, **43–44**, 77–93, https://doi.org/10.1016/j.ocemod.2011.12.003.

——, P. J. S. Franks, and K. S. Smith, 2018: The role of submesoscale currents in structuring marine ecosystems. *Nat. Commun.*, **9**, 4758, https://doi.org/10.1038/s41467-018-07059-3.

Mahadevan, A., 2014: Eddy effects on biogeochemistry. *Nature*, **506**, 168–169, https://doi.org/10.1038/nature13048.

Marshall, J., E. Shuckburgh, H. Jones, and C. Hill, 2006: Estimates and implications of surface eddy diffusivity in the Southern Ocean derived from tracer transport. *J. Phys. Oceanogr.*, **36**, 1806–1821, https://doi.org/10.1175/JPO2949.1.

McDougall, T. J. and P. M. Barker, 2011: Getting started with TEOS-10 and the Gibbs Seawater (GSW) Oceanographic Toolbox, version 3.06. SCOR/IAPSO WG127, 28 pp., http://www.teos-10.org/pubs/Getting_Started.pdf.

McWilliams, J. C., 2016: Submesoscale currents in the ocean. *Pro. Roy. Soc. London*, **472A**, 20160117, https://doi.org/10.1098/rspa.2016.0117.

Mensa, J. A., Z. Garraffo, A. Griffa, T. M. Özgökmen, A. Haza, and M. Veneziani, 2013: Seasonality of the submesoscale dynamics in the Gulf Stream region. *Ocean Dyn.*, **63**, 923–941, https://doi.org/10.1007/s10236-013-0633-1.

Munk, W., 1981: Internal waves and small-scale processes. *Evolution of Physical Oceanography*, B. A. Warren and C. Wunsch, Eds., MIT Press, 264–291.

——, and N. Phillips, 1968: Coherence and band structure of inertial motion in the sea. *Rev. Geophys.*, **6**, 447–472, https://doi.org/10.1029/RG006i004p00447.

——, and C. Wunsch, 1998: Abyssal recipes II: Energetics of tidal and wind mixing. *Deep-Sea Res. I*, **45**, 1977–2010, https://doi.org/10.1016/S0967-0637(98)00070-3.

Polzin, K. L., and Y. V. Lvov, 2011: Toward regional characterizations of the oceanic internal wavefield. *Rev. Geophys.*, **49**, https://doi.org/10.1029/2010RG000329.

Ponte, A. L., P. Klein, M. Dunphy, and S. L. Gentil, 2017: Low-mode internal tides and balanced dynamics disentanglement in altimetric observations: Synergy with surface density observations. *J. Geophys. Res. Oceans*, **122**, 2143–2155, https://doi.org/10.1002/2016JC012214.

Qiu, B., T. Nakano, S. Chen, and P. Klein, 2017: Submesoscale transition from geostrophic flows to internal waves in the northwestern Pacific upper ocean. *Nat. Commun.*, **8**, 14055, https://doi.org/10.1038/ncomms14055.

——, S. Chen, P. Klein, J. Wang, H. Torres, L.-L. Fu, and D. Menemenlis, 2018: Seasonality in transition scale from balanced to unbalanced motions in the world ocean. *J. Phys. Oceanogr.*, **48**, 591–605, https://doi.org/10.1175/JPO-D-17-0169.1.

Rainville, L., and R. Pinkel, 2006: Propagation of low-mode internal waves through the ocean. *J. Phys. Oceanogr.*, **36**, 1220–1236, https://doi.org/10.1175/JPO2889.1.

Ray, R. D., and G. T. Mitchum, 1997: Surface manifestation of internal tides in the deep ocean: Observations from altimetry and island gauges. *Prog. Oceanogr.*, **40**, 135–162, https://doi.org/10.1016/S0079-6611(97)00025-6.

——, and E. D. Zaron, 2011: Non-stationary internal tides observed with satellite altimetry. *Geophys. Res. Lett.*, **38**, L17609, https://doi.org/10.1029/2011GL048617.

——, and ——, 2016: M2 internal tides and their observed wavenumber spectra from satellite altimetry. *J. Phys. Oceanogr.*, **46**, 3–22, https://doi.org/10.1175/JPO-D-15-0065.1.

Richman, J. G., B. K. Arbic, J. F. Shriver, E. J. Metzger, and A. J. Wallcraft, 2012: Inferring dynamics from the wavenumber spectra of an eddying global ocean model with embedded tides. *J. Geophys. Res.*, **117**, C12012, https://doi.org/10.1029/2012JC008364.

Rocha, C. B., T. K. Chereskin, S. T. Gille, and D. Menemenlis, 2016a: Mesoscale to submesoscale wavenumber spectra in Drake Passage. *J. Phys. Oceanogr.*, **46**, 601–620, https://doi.org/10.1175/JPO-D-15-0087.1.

——, S. T. Gille, T. K. Chereskin, and D. Menemenlis, 2016b: Seasonality of submesoscale dynamics in the Kuroshio Extension. *Geophys. Res. Lett.*, **43**, 11 304–11 311, https://doi.org/10.1002/2016GL071349.

Sasaki, H., and P. Klein, 2012: SSH wavenumber spectra in the North Pacific from a high-resolution realistic simulation. *J. Phys. Oceanogr.*, **42**, 1233–1241, https://doi.org/10.1175/JPO-D-11-0180.1.

——, ——, B. Qiu, and Y. Sasai, 2014: Impact of oceanic-scale interactions on the seasonal modulation of ocean dynamics by the atmosphere. *Nat. Commun.*, **5**, 5636, https://doi.org/10.1038/ncomms6636.

Savage, A. C., and Coauthors, 2017a: Frequency content of sea surface height variability from internal gravity waves to mesoscale eddies. *J. Geophys. Res. Oceans*, **122**, 2519–2538, https://doi.org/10.1002/2016JC012331.

——, and Coauthors, 2017b: Spectral decomposition of internal gravity wave sea surface height in global models. *J. Geophys. Res. Oceans*, **122**, 7803–7821, https://doi.org/10.1002/2017JC013009.

Shcherbina, A. Y., E. A. D'Asaro, C. M. Lee, J. M. Klymak, M. J. Molemaker, and J. C. McWilliams, 2013: Statistics of vertical vorticity, divergence, and strain in a developed submesoscale turbulence field. *Geophys. Res. Lett.*, **40**, 4706–4711, https://doi.org/10.1002/grl.50919.

Simmons, H. L., R. W. Hallberg, and B. K. Arbic, 2004: Internal wave generation in a global baroclinic tide model. *Deep-Sea Res. II*, **51**, 3043–3068, https://doi.org/10.1016/j.dsr2.2004.09.015.

Stammer, D., 1998: On eddy characteristics, eddy transports, and mean flow properties. *J. Phys. Oceanogr.*, **28**, 727–739, https://doi.org/10.1175/1520-0485(1998)028<0727:OECETA>2.0.CO;2.

——, and A. Cazenave, Eds., 2017: *Satellite Altimetry Over Oceans and Land Surfaces*. CRC Press, 644 pp.

——, and Coauthors, 2014: Accuracy assessment of global barotropic ocean tide models. *Rev. Geophys.*, **52**, 243–282, https://doi.org/10.1002/2014RG000450.

Su, Z., J. Wang, P. Klein, A. F. Thompson, and D. Menemenlis, 2018: Open submesoscales as a key component of the global heat budget. *Nat. Commun.*, **9**, 775, https://doi.org/10.1038/s41467-018-02983-w.

Thomas, L. N., A. Tandon, and A. Mahadevan, 2008: Submesoscale processes and dynamics. *Ocean Modeling in an Eddying Regime*, *Geophys. Monogr.*, Vol. 177, Amer. Geophys. Union, 17–38.

Thompson, A. F., A. Lazar, C. Buckingham, A. C. Naveira Garabato, G. M. Damerell, and K. J. Heywood, 2016: Open-ocean submesoscale motions: A full seasonal cycle of mixed layer instabilities from gliders. *J. Phys. Oceanogr.*, **46**, 1285–1307, https://doi.org/10.1175/JPO-D-15-0170.1.

Tulloch, R., J. Marshall, C. Hill, and K. S. Smith, 2011: Scales, growth rates, and spectral fluxes of baroclinic instability in the ocean. *J. Phys. Oceanogr.*, **41**, 1057–1076, https://doi.org/10.1175/2011JPO4404.1.

Wang, D.-P., C. N. Flagg, K. Donohue, and H. T. Rossby, 2010: Wavenumber spectrum in the Gulf Stream from shipboard ADCP observations and comparison with altimetry measurements. *J. Phys. Oceanogr.*, **40**, 840–844, https://doi.org/10.1175/2009JPO4330.1.

Wang, J., L. Fu, H. S. Torres, S. Chen, B. Qiu, and D. Menemenlis, 2019: On the spatial scales to be resolved by the surface water and ocean topography Ka-band radar interferometer. *J. Atmos. Oceanic Technol.*, **36**, 87–99, https://doi.org/10.1175/JTECH-D-18-0119.1.

Wunsch, C., 1997: The vertical partition of oceanic horizontal kinetic energy. *J. Phys. Oceanogr.*, **27**, 1770–1794, https://doi.org/10.1175/1520-0485(1997)027<1770:TVPOOH>2.0.CO;2.

——, 2013: Baroclinic motions and energetics as measured by altimeters. *J. Atmos. Oceanic Technol.*, **30**, 140–150, https://doi.org/10.1175/JTECH-D-12-00035.1.

——, and A. E. Gill, 1976: Observations of equatorially trapped waves in Pacific sea level variations. *Deep-Sea Res. Oceanogr. Abstr.*, **23**, 371–390, https://doi.org/10.1016/0011-7471(76)90835-4.

——, and D. Stammer, 1998: Satellite altimetry, the marine geoid, and the oceanic general circulation. *Annu. Rev. Fluid Mech.*, **26**, 219–253 https://doi.org/10.1146/annurev.earth.26.1.219.

Xu, Y., and L.-L. Fu, 2011: Global variability of the wavenumber spectrum of oceanic mesoscale turbulence. *J. Phys. Oceanogr.*, **41**, 802–809, https://doi.org/10.1175/2010JPO4558.1.

——, and ——, 2012: The effects of altimeter instrument noise on the estimation of the wavenumber spectrum of sea surface height. *J. Phys. Oceanogr.*, **42**, 2229–2233, https://doi.org/10.1175/JPO-D-12-0106.1.

Zanifé, O. Z., P. Vincent, L. Amarouche, J. P. Dumont, P. Thibaut, and S. Labroue, 2003: Comparison of the Ku-band range noise level and the relative sea-state bias of the Jason-1, TOPEX, and Poseidon-1 radar altimeters. *Mar. Geod.*, **26**, 201–238, https://doi.org/10.1080/714044519.

Zaron, E. D., 2017: Mapping the nonstationary internal tide with satellite altimetry. *J. Geophys. Res. Oceans*, **112**, 539–554, https://doi.org/10.1002/2016JC012487.

——, and G. D. Egbert, 2014: Time-variable refraction of the internal tide at the Hawaiian Ridge. *J. Phys. Oceanogr.*, **44**, 538–557, https://doi.org/10.1175/JPO-D-12-0238.1.

Zhao, Z., 2016: Internal tide oceanic tomography. *Geophys. Res. Lett.*, **43**, 9157–9164, https://doi.org/10.1002/2016GL070567.

——, M. H. Alford, J. B. Girton, L. Rainville, and H. L. Simmons, 2016: Global observations of open-ocean mode-1 M2 internal tides. *J. Phys. Oceanogr.*, **46**, 1657–1684, https://doi.org/10.1175/JPO-D-15-0105.1.